Multi-channel modelling approach for particulate filters

Prantoni, M, Aleksandrova, S, Medina, H & Benjamin, S

Contents lists available at ScienceDirect

Results in Engineering

journal homepage: www.editorialmanager.com/rineng/Default.aspx

Multi-channel modelling approach for particulate filters

M. Prantoni [*], S. Aleksandrova, H. Medina, S. Benjamin

Coventry University, UK

ABSTRACT

The reduction of transport particulate matter emissions is crucial for improving air quality. Although particulate filters are efficient in removal of particulate matter, their inclusion in modern exhaust systems results in high back pressures and thus higher fuel consumption. Consequently, there is an ever-increasing demand within the automotive industry for more accurate and reliable filter design tools. A common modelling approach is to use 0-, 1- and 2-dimensional simplified filter flow models as part of the entire exhaust system. These models fail to capture the intrinsically 3-dimensional complex flow features present in the exhaust systems. In this work, a multi-channel modelling approach is implemented for the first time to provide full coupling within a CFD simulation framework. The strength of the new methodology is that it offers for the first time the ability to: (i) capture channel-to-channel flow interactions, (ii) account for density variations within individual channels, and (iii) investigate the overall effect of a given filter configuration on the exhaust system in 3D (i.e. upstream and downstream effects). The method retains the simplicity of a 1-dimensional filter channel model while providing an insight into the 3-dimensional non-uniform flow distribution between the channels. This approach represents an important new tool for exhaust system design and optimisation.

Introduction

Particulate Matter (PM) emissions from internal combustion engines are extremely harmful for the human health and the environment [1–3]. In order to mitigate the problem, automotive companies use diesel or gasoline particulate filters (DPFs or GPFs), which are considered a standard and proven technology for the control of soot particle emissions [4]. Filters can also be used as catalysts at the same time, in which case a catalyst coating is applied to the filter walls. Most of the filters on the market have wall-flow geometry, where the exhaust gas is forced through the porous walls of the filter. However, integration of the wall-flow filter in the exhaust system produces a high backpressure, and the engine must provide extra work to overcome it. This affects the performance of the engine, in particular its fuel efficiency. Therefore, the ability to accurately predict the backpressure caused by the filter monolith has become very important for automotive companies in the optimisation of their vehicles [5].

The first significant study of particulate filter modelling was presented by Bissett [6] in 1984. Bissett proposed a simple 1-dimensional model, with the aim to gain a deeper understanding of the regeneration process in wall-flow diesel particulate filters. The formulation of this model was successively adopted by many authors as a basis for the development of several predictive models (0-, 1- and 2-dimensional) more focused on the pressure drop or filtration efficiency characteristics of the filters. A review of most of these models can be found in Refs. [7–9], while most recently published studies can be found in Refs. [5, 10–12].

The majority of these models are based on a scaling approach through which the pressure drop of the filter can be modelled by considering a simplified geometry including only a single inlet and outlet channel. As reported in Ref. [6], the approximation introduced through the scaling approach can be justified when the velocity profile entering the filter is flat, so that the mass flow rate is the same in all channels, and when the ratio between the cell hydraulic diameter and the filter diameter is very small ($d_h/D_{Filter} \ll 1$), so that the full coupling between open and closed channels is negligible on the scale of the entire filter. The applicability of the scaling approach is also limited to filters with homogeneous properties (i.e. all the cells have the same hydraulic diameter, all the porous walls have the same permeability, and soot is distributed homogeneously).

However, in most of the applications the velocity profile upstream the filter is likely to be non-uniform. This is due to a combination of different

factors such as: a) the concentric or eccentric expansion upstream the filter, present in most aftertreatment systems because of the different diameter between the exhaust pipeline and the filter, b) a non-uniform soot loading, c) a non-uniform wall permeability, often present in coated filters due to the non-homogeneous deposit of catalyst coating material in different channels, d) a swirling flow upstream the filter, which might be present in turbo- or super-charged systems. In these conditions, accurate modelling of the particulate filter flow is much more challenging, not only because of the flow exchange between neighbouring channels, which should be taken into account, but also, and most importantly, because the flow profile upstream the filter cannot be known a priori.

Several attempts have been made to model flow in multiple channel geometries. Full 3-dimensional CFD studies (e.g. Ref. [13]), 2-dimensional approximations [14], lumped model approach [15] have been used. Most of the existing multi-channel models [4,14,16–18] are based on the 1-dimensional model derived from work of Bisset [6] and Konstandopoulos [19]. However, all these methods require a known velocity profile upstream the filter, and many do not take into account the full cross-flow between the channels, instead modelling the filter as a collection of inlet/outlet channel pairs. Some studies assume uniform pressure upstream instead of uniform flow [13], which is also limiting the flow configuration as the pressure distribution upstream of aftertreatment devices with expansion is also highly non-uniform due to the high velocity central flow impinging onto the middle part of the monolith (as shown later in this paper).

The assumption of uniform flow distribution upstream is based on the fact that the filter is often preceded by a catalyst which makes the flow more uniform (e.g. Ref. [13]). However, even in these conditions the flow through catalyst is often highly non-uniform [20] due to the presence of an expansion immediately upstream. If present, an upstream turbine would also affect the flow entering the catalyst (see, e.g. Ref. [21]) and, consequently, the filter downstream. Other factors affecting flow distribution between the channels can include: (i) differences in channel wall permeability (due to soot/ash accumulation and uneven catalyst coating distribution), (ii) channel geometry (for example, manufacturing defects), and (iii) radial temperature gradients. Therefore, ability to model filters with uneven flow distribution between the channels is essential for accurate predictions of filter performance.

This work presents a fully coupled multi-channel model based on the 1-dimensional formulation introduced by Konstandopoulos [19], and demonstrates how it can be coupled with a 3D computational fluid dynamics (CFD) simulation. The channel flow solution is obtained in Matlab, and the commercial CFD package Star-CCM+ is used here. However, the same approach can be readily used with any other boundary value problem solver and CFD software. The proposed multi-channel model takes into account both the cross-flow between channels and the non-uniform flow distribution upstream of the filter. The 3-dimensional flow upstream of the filter is coupled to the filter flow, so that no prior knowledge of the upstream flow is needed. Density variation in the channels due to high pressure is also taken into account, and non-uniform channel properties (along the channel and between different channels) can be accounted for.

Apart from the global flow features and total pressure loss, the proposed model provides details of the flow and pressure distribution in the filter channels. These are of course limited to the 1-dimensional approximation, but are still highly valuable for particulate filter optimisation, since, as reported by Piscaglia: "The particulate filters performance is studied in terms of pressure drop, regeneration, collection efficiency, creation, distribution and deposition of ash; many of these phenomena are driven or highly influenced by the hydrodynamics of the filter" [22].

Multi-channel model development and coupling with CFD

Multi-channel model formulation

A wall-flow filter channel geometry considered here is the same as discussed in previous works such as [19] or [5]. Although the model can be used for filters with any cross-section, a circular cross-section will be used here for simplicity. A sketch of a typical filter frontal area is shown in Fig. 1. A two-dimensional indexing system (i,j) is used to refer to the filter channels. Note that in Fig. 1 the j index is reversed to be consistent with the notation of Fig. 2. The indexing scheme (Fig. 2) reflects that every open channel (in white) has an even sum of indices and every closed channel (in grey) has an odd sum of indices.

The equations governing the flow in the (i,j) channel can be written as follows, in accordance with the notation shown in Fig. 2:

Inlet channels$(i+j=$ even$)$ & outlet channels$(i+j=$ odd$)$

Mass balance:

$$\frac{d}{dx}\left(\rho_{i,j}u_{i,j}\right) = -\xi\frac{1}{d_h}\rho_{i,j}\left(v_{i,j}+w_{i,j}+v_{i+1,j}+w_{i,j+1}\right) \tag{1}$$

Momentum balance:

$$\frac{d}{dx}\left(\rho_{i,j}u_{i,j}^2\right) = -\frac{d}{dx}\left(P_{i,j}\right) - 2fRe\frac{\mu}{d_h^2}u_{i,j} \tag{2}$$

Wall pressure drop:

$$P_{i,j} - P_{i-1,j} = \xi\,P_{i,j}\left(\frac{2}{P_{i,j}+P_{i-1,j}}\right)\,\frac{\mu}{\tau_{i,j}}t_{i,j}v_{i,j} \tag{3}$$

$$P_{i,j} - P_{i,j-1} = \xi\,P_{i,j}\left(\frac{2}{P_{i,j}+P_{i,j-1}}\right)\,\frac{\mu}{\sigma_{i,j}}s_{i,j}w_{i,j} \tag{4}$$

$$P_{i,j} - P_{i+1,j} = \xi\,P_{i,j}\left(\frac{2}{P_{i,j}+P_{i+1,j}}\right)\,\frac{\mu}{\tau_{i+1,j}}t_{i+1,j}v_{i+1,j} \tag{5}$$

$$P_{i,j} - P_{i,j+1} = \xi\,P_{i,j}\left(\frac{2}{P_{i,j}+P_{i,j+1}}\right)\,\frac{\mu}{\sigma_{i,j+1}}s_{i,j+1}w_{i,j+1} \tag{6}$$
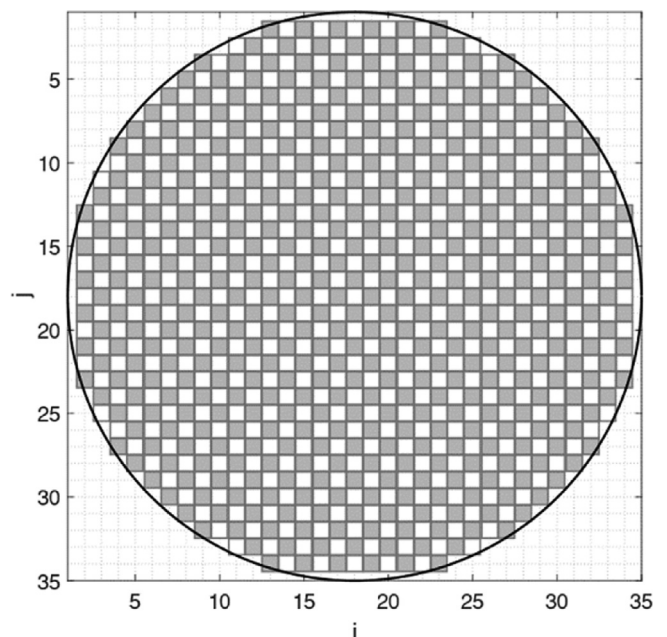

Fig. 1. Schematic of cell Indexing order.

Here:

- $u_{i,j}$ is the mean cross-sectional axial velocity in the (i,j) channel,
- $P_{i,j}$ is the mean cross-sectional pressure in the (i,j) channel,
- $v_{i,j}$ and $w_{i,j}$ are the superficial velocities through the "vertical" and "horizontal" walls respectively as shown in Fig. 2,

$$\rho_{i,j} = \frac{P_{i,j}}{R_{Gas} T}. \tag{7}$$

where R_{Gas} is the specific gas constant.

Eqs (1)–(6) can be rearranged to give the following differential equations for mass and momentum balance:

$$\frac{d}{dx}(u_{i,j}) = \frac{1}{\left(1 - \frac{1}{1+\frac{1}{R_{Gas}T}u_{i,j}^2} \frac{2}{R_{Gas}T} u_{i,j}^2\right)} \left[\frac{1}{P_{i,j}}\left(\frac{1}{1+\frac{1}{R_{Gas}T}u_{i,j}^2}\right) 2fRe\frac{\mu}{d_h^2}u_{i,j}^2 \right.$$
$$\left. - \frac{1}{P_{i,j}}\frac{1}{d_h}\frac{1}{2\mu}\left(\frac{\tau_{i,j}}{t_{i,j}}\left(P_{i,j}^2 - P_{i-1,j}^2\right) + \frac{\sigma_{i,j}}{s_{i,j}}\left(P_{i,j}^2 - P_{i,j-1}^2\right) + \frac{\tau_{i+1,j}}{t_{i+1,j}}\left(P_{i,j}^2 - P_{i+1,j}^2\right) + \frac{\sigma_{i,j+1}}{s_{i,j+1}}\left(P_{i,j}^2 - P_{i,j+1}^2\right)\right) \right] \tag{8}$$

$$\frac{d}{dx}(P_{i,j}) = \frac{1}{1+\frac{1}{R_{Gas}T}u_{i,j}^2}\left\{ -\frac{2}{R_{Gas}T}P_{i,j}u_{i,j}\left\{ \frac{1}{\left(1 - \frac{1}{1+\frac{1}{R_{Gas}T}u_{i,j}^2}\frac{2}{R_{Gas}T} u_{i,j}^2\right)}\left[\frac{1}{P_{i,j}}\left(\frac{1}{1+\frac{1}{R_{Gas}T}u_{i,j}^2}\right)2fRe\frac{\mu}{d_h^2}u_{i,j}^2 \right. \right. \right.$$
$$\left. \left. \left. - \frac{1}{P_{i,j}}\frac{1}{d_h}\frac{1}{2\mu}\left(\frac{\tau_{i,j}}{t_{i,j}}\left(P_{i,j}^2 - P_{i-1,j}^2\right) + \frac{\sigma_{i,j}}{s_{i,j}}\left(P_{i,j}^2 - P_{i,j-1}^2\right) + \frac{\tau_{i+1,j}}{t_{i+1,j}}\left(P_{i,j}^2 - P_{i+1,j}^2\right) + \frac{\sigma_{i,j+1}}{s_{i,j+1}}\left(P_{i,j}^2 - P_{i,j+1}^2\right)\right) \right] \right\} - 2fRe\frac{\mu}{d_h^2}u_{i,j} \right\} \tag{9}$$

- $\rho_{i,j}$ is the mean cross-sectional density in the (i,j) channel,
- μ is the gas dynamic viscosity,
- $t_{i,j}$ and $s_{i,j}$ are the thicknesses of the "vertical" and "horizontal" walls respectively as sown in Fig. 2,
- $\tau_{i,j}$ and $\sigma_{i,j}$ are the permeabilities of the vertical and horizontal walls respectively,
- ξ is a coefficient equal to $\xi = 1$ for the inlet channels and $\xi = -1$ for the outlet channels, and can be expressed as $\xi = (-1)^{i+j}$,
- d_h is the cell hydraulic diameter,
- f is the Fanning friction factor,
- Re is the channel Reynolds number (defined as $Re = \frac{\rho U d_h}{\mu}$),
- x is the axial coordinate, varying from 0 at the entrance of the filter to L at the exit of the filter.

Thus, the present formulation allows the wall thickness and wall permeability to be varied in selected cells. Note that wall thickness and other parameters can also be functions of the axial coordinate. For simplicity, they are assumed constant in axial direction in this initial study aimed at demonstration of the approach.

Eqs. (3)–(6) come from solving the differential form of Darcy's law to allow for the change in gas density through the filter wall as suggested by Konstandopoulos [23] (see Appendix). The hydraulic diameter of selected cells could also be varied by using (i,j) indexing system for cell size definition. However, this would require a different form of Darcy's law to account for the trapezoidal cross-section of the walls, which has not been included for the present study.

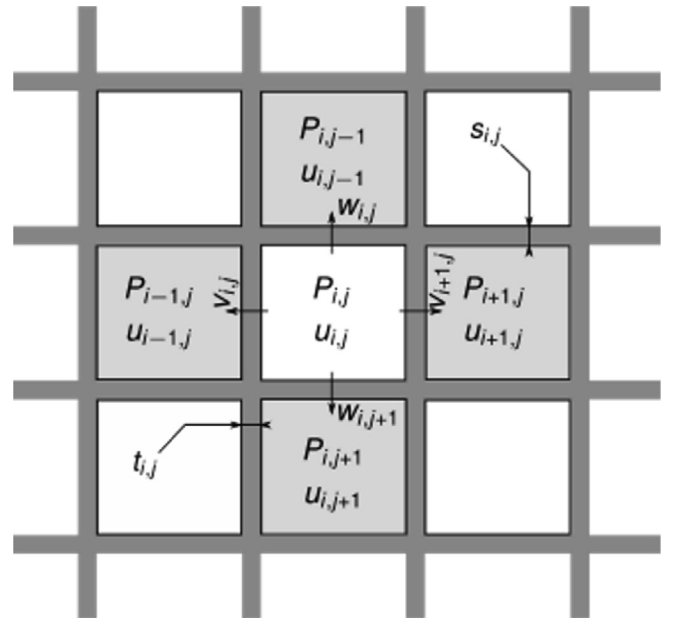In accordance with the ideal gas law, the local density can be defined as:

Fig. 2. Flow variable numbering.

Thus, for each channel (inlet or outlet) the two unknown functions (mean axial velocity and pressure) satisfy first order non-linear differential eqs (8) and (9). The problem in each channel is coupled with the four neighbouring channels. Treatment of the channels with fewer neighbours is discussed below.

The boundary conditions for the system use the known velocity entering the inlet channel, zero velocity at the end of the inlet channel and beginning of the outlet channel, and a known pressure at the end of the outlet channel:

Inlet channels $(i + j = \mathbf{even})$

$$u_{i,j}(x = 0) = U_{i,j} \tag{10}$$

$$u_{i,j}(x = L) = 0 \tag{11}$$

Outlet channels $(i + j = \mathbf{odd})$

$$u_{i,j}(x = 0) = 0 \tag{12}$$

$$P_{i,j}(x = L) = P_{Outlet} \tag{13}$$

where:

- $U_{i,j}$ is the mean axial velocity at the entrance of the inlet channel (i, j),
- P_{Outlet} is the pressure at the exit of the outlet channel.

In the above, $U_{i,j}$ can either be assigned by assuming a velocity profile upstream the filter a priori (in this case there is no need for the coupling with the CFD) or, as in this study, it can be determined using CFD simulations. Although other authors used the former approach (e.g. Ref. [16]), due to the elliptic nature of the Navier-Stokes equations the latter method is more rigorous.

The additional boundary conditions for the left, top, right and bottom impermeable walls of the channels at the border of the filter are respectively:

$$P_{i,j} - P_{i-1,j} = 0 \tag{14}$$

$$P_{i,j} - P_{i,j-1} = 0 \tag{15}$$

$$P_{i,j} - P_{i+1,j} = 0 \tag{16}$$

$$P_{i,j} - P_{i,j+1} = 0 \tag{17}$$

which reflect the fact that the superficial velocity ($v_{i,j}$, $w_{i,j}$, $v_{i+1,j}$ and $w_{i,j+1}$) through these walls is zero.

For a given geometry (e.g. the one shown in Fig. 1), the resultant system of coupled differential equations can be solved numerically using a boundary value problem solver. In the present study, the multi-channel model has been implemented in Matlab and the boundary value problem solver bvp5c has been used to solve the system of coupled differential eqs (8) and (9) subject to boundary conditions (10)–(13) and extra algebraic eqs (14)–(17). The solver is a finite difference code that implements the four-stage Lobatto IIIa formula [24]. This solver is not parallelised, which was not crucial for the small-scale cases considered here, but parallel versions of the solver are also available. Once axial velocity and pressure distribution for each channel is known, superficial velocities can also be calculated using eqs (3) – (6).

As suggested by Konstandopoulos [6], the contribution of the contraction and expansion irreversible losses can be added in series to the filter pressure drop. The irreversible contraction and expansion losses can be calculated with the following approximations:

$$\Delta P_{Contr.} = \zeta_{Contr.} \frac{\sum_{n_{Inlet}} \left(\frac{\rho_{i,j\ Inlet}\ u_{i,j\ Inlet}^2}{2} \right)}{n_{Inlet}} \tag{18}$$

$$\Delta P_{Exp.} = \zeta_{Exp.} \frac{\sum_{n_{Outlet}} \left(\frac{\rho_{i,j\ Outlet}\ u_{i,j\ Outlet}^2}{2} \right)}{n_{Outlet}} \tag{19}$$

where:

- $u_{i,j\ Inlet}$ and $u_{i,j\ Outlet}$ are the mean cross-sectional axial velocities at the inlet and outlet of the (i, j) channel, respectively,
- $\rho_{i,j\ Inlet}$ and $\rho_{i,j\ Outlet}$ are the mean cross-sectional densities at the inlet and outlet of the (i, j) channel, respectively,
- n_{Inlet} and n_{Outlet} are the number of inlet and outlet channels, respectively,
- $\zeta_{Contr.}$ and $\zeta_{Exp.}$ are the contraction [25] and expansion coefficients [26], defined as in eqs (26) and (27).

$$\zeta_{Contr.} = 0.5 \left(1 - \frac{A_1}{A_2} \right) \tag{20}$$

$$\zeta_{Exp.} = \left(1 - \frac{A_1}{A_2} \right)^2 \tag{21}$$

where A_1 is the open frontal area of the filter and A_2 is the total frontal area of the filter.

The total pressure drop across the filter can be calculated as the surface averaged absolute pressure at the entrance faces of the inlet open channels minus the surface averaged absolute pressure at the exit faces of the outlet channels, together with the irreversible losses from sudden contraction and expansion.

CFD methodology

In order to demonstrate how the multi-channel model can be combined with CFD calculations, several simple geometries representative of typical exhaust systems have been considered using StarCCM+. The computational domain comprises an inlet section followed by a sudden expansion (Fig. 3). Filter diameter of 50 mm has been chosen because experimental measurements from Ref. [5] are used for validation purposes. Other dimensions have been chosen arbitrary for demonstration purposes. A mass flow rate of 30 g/s is prescribed at the geometry inlet section. The filter is not included in the computational domain, but the entrance faces of the inlet channels are included and set up as pressure
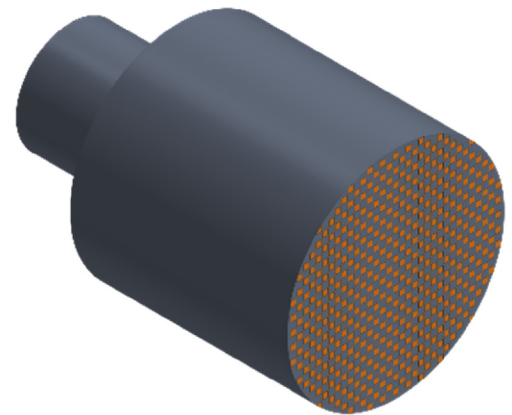

Fig. 3. A sample CFD computational domain.

Table 1
StarCCM + set up parameters.

| Parameter	Model
Geometry/Domain	3-D
Time	Steady State
Flow Solver	Segregated Flow
Viscous Regime	Turbulent
RANS Turbulent Model	v2f
Convection Scheme	2nd-order
Temperature	Isothermal, $T = 680\,[^\circ C]$
Equation of State	Ideal Gas Law
Fluid Dynamic Viscosity	Sutherland's Law $\mu = \mu_{ref} \left(\dfrac{T}{T_{ref}}\right)^{3/2} \dfrac{T_{ref} + S}{T + S}\left[\dfrac{Kg}{m\,s}\right]$,
	$T = 953.15[K]$, $T_{ref} = 273.15[K]$, $\mu_{ref} = 1.716 \times 10^{-5}\left[\dfrac{Kg}{m\,s}\right]$ and
	$S = 110.4[K]$

outlets (Fig. 3). The value of the pressure for each filter channel is determined from the multi-channel model and is discussed in the next section. The remaining boundary surfaces are set up as no slip walls.

The additional set-up details for the simulations are reported in Table 1. Turbulence model v2f has been chosen as it has been shown to perform reasonably well in separated flows [20]. Temperature of $680^\circ C$ is used to enable comparison with the experimental data published in Ref. [5].

A polyhedral mesh was used for domain discretisation, with 10 prism layers near the walls to achieve y + values below 1. A mesh independence study has been carried out to ensure a mesh-independent solution.

Multi-channel model and CFD coupling methodology

The multi-channel and CFD models are coupled through the front
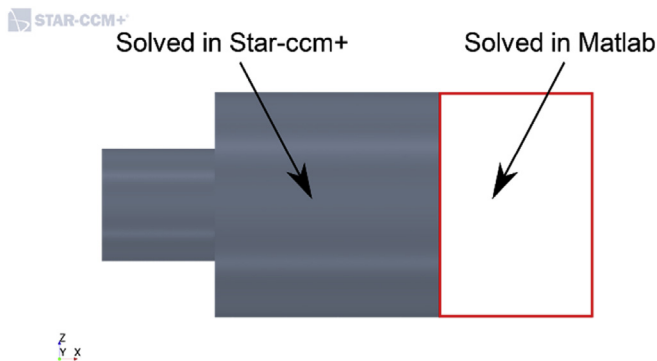
Fig. 4. Computational domain used in StarCCM+ (inlet section and expansion) and Matlab (filter channels).
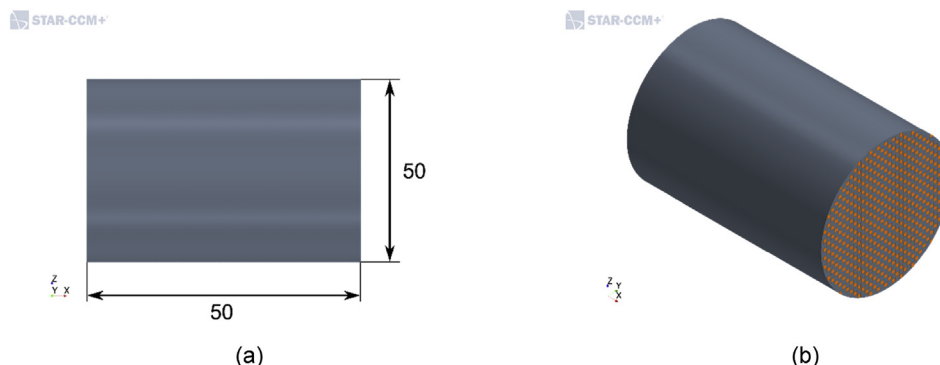
faces of the inlet channels (Fig. 4), and an iteration procedure is used to obtain a converged solution in both domains. The following solution process has been used here:

1) Setup CFD simulation in StarCCM+, with initial pressures at the inlet channel entrances estimated from the analytical solution of the one-dimensional model from Ref. [19].
2) Run the CFD simulation until convergence.
3) Extract the mass flow rate and density from each entrance face of the inlet channels and calculate the mean cross-sectional velocity entering each channel ($U_{i,j} = \frac{\dot{m}_{i,j}}{d_h^2\,\rho_{i,j}}$).
4) Use these velocities as inlet boundary conditions for the multi-channel model and solve the boundary value problem using Matlab. The pressure at the exit of the outlet channels is set as ambient pressure here because the flow downstream the filter is not considered, but would generally need to be coupled with the downstream solution.
5) Extract pressure at the entrance of each inlet channel from the model solution.
6) Update the outlet pressure boundary condition of each entrance face of the inlet channels in the CFD simulation with the newly calculated backpressure.
7) Steps 2) to 6) are repeated n times, until the difference in back-pressure of each single channel between two successive iterations is lower that 0.1%, which is the criterion selected for the convergence here.

In order to improve stability and convergence time (that is around 10 h per case, of which 2/3 of the time is taken by the multi-channel model solution in Matlab), a limiter was applied to the pressure correction between iterations. If the calculated correction for the pressure at the entrance to the inlet channels exceeded 1% of the absolute pressure value, only 1% correction was used. In the multi-channel model, the 1-dimensional solution from the model by Konstandopoulos [19] was used as the initial guess.

Thus, the CFD and multi-channel models are fully coupled and the velocity profile entering the filter is not assumed a priori. This accounts for the fact that the velocity profile entering the filter is affected by both the uneven backpressure from different channels and the configuration of the geometry upstream the filter.

Results

Bare and coated filters

The two cases presented in this section include a bare and a catalyst coated filter cores. Experimental measurements for these configurations have been reported in Ref. [5] and are used here for an initial assessment of the multi-channel model approach. A simple configuration with no


(a)

(b)

Fig. 5. CFD computational domain for bare and coated core experimental validation: (a) side view and (b) isometric view. Dimensions in [mm].

Table 2
Filter properties.

Property	Unit	Bare Filter	Coated Filter
Cell density	[Cpsi]	300	300
Length	[mm]	125	125
Filter diameter	[mm]	50	50
Cell hydraulic diameter	[mm]	1.26	1.22
Uncoated wall thickness	[mm]	0.203	0.203
Coating layer thickness	[mm]	0	0.035
Total wall thickness	[mm]	0.203	0.238
Estimated permeability	[m^2]	5.5×10^{-12}	1.9×10^{-13}

sudden expansion is used to replicate the experimental conditions (Fig. 5), and filter properties used for calculations are identical to the ones in Ref. [5] (see Table 2), including the permeability values estimated from the experimental measurements. Note that the method of permeability estimation from the experiments is based on the assumption

that the filter permeability is homogeneous. This condition is generally accepted to be true for bare filters. However, catalyst-coated filters may present different coating thickness and penetration depth in different regions of the filter, thus modifying the local permeability of the filter. For the two test cases presented in this section the permeability of the filters has been assumed homogeneous, while the effect of non-homogeneous permeability is investigated in the last two test cases.

The multi-channel model computational domain includes 437 inlet channels and 448 outlet channels, for a total of 885 channels. Since the numerical solution of the system of differential equations with bvp5c requires a discretisation of each channel along its axial direction, a mesh dependency study for the bare and coated filter has been carried out. It has been found that 31 mesh points for the bare filter and 11 mesh points for the coated one are sufficient to reach independence of the solutions. Note that these values may change if a solver other than bvp5c is used. The difference in the number of mesh points required to reach independence of the solutions is caused by the marked difference in the
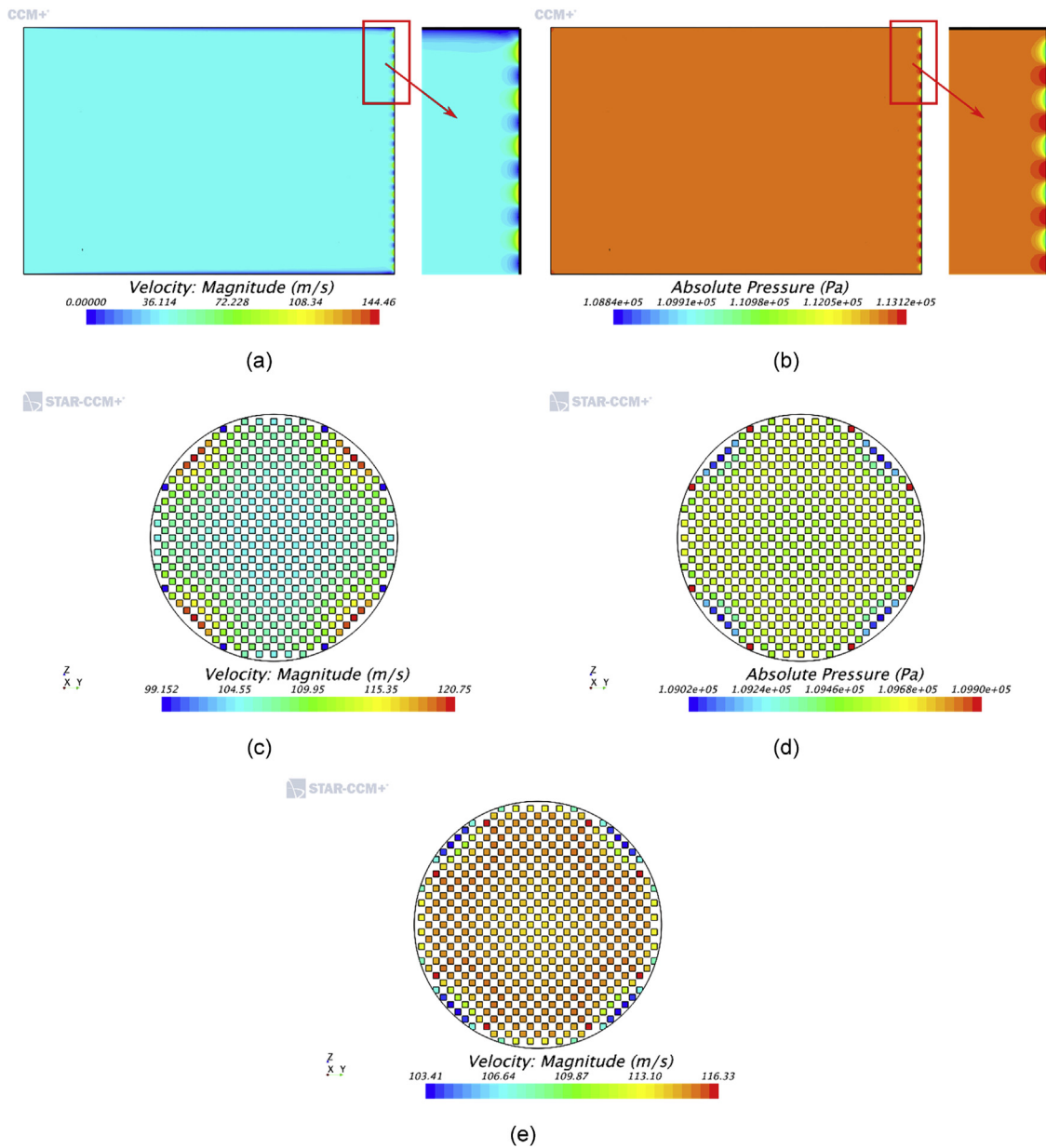
Fig. 6. Results for 300/8 bare filter: (a) Velocity magnitude in the mid-section of the CFD domain (with the flow going from the left to the right), (b) Absolute pressure in the mid-section of the CFD domain, (c) Mean channel velocity at the entrance of each inlet channel (from the Matlab domain), (d) Mean channel pressure at the entrance of each inlet channel (from the Matlab domain), (e) Mean channel velocity at the exit of each outlet channel (from the Matlab domain).

Fig. 7. Results for 300/8 coated filter: (a) Velocity magnitude in the mid-section of the CFD domain (with the flow going from the left to the right), (b) Absolute pressure in the mid-section of the CFD domain, (c) Mean channel velocity at the entrance of each inlet channel (from the Matlab domain), (d) Mean channel pressure at the entrance of each inlet channel (from the Matlab domain), (e) Mean channel velocity at the exit of each outlet channel (from the Matlab domain).
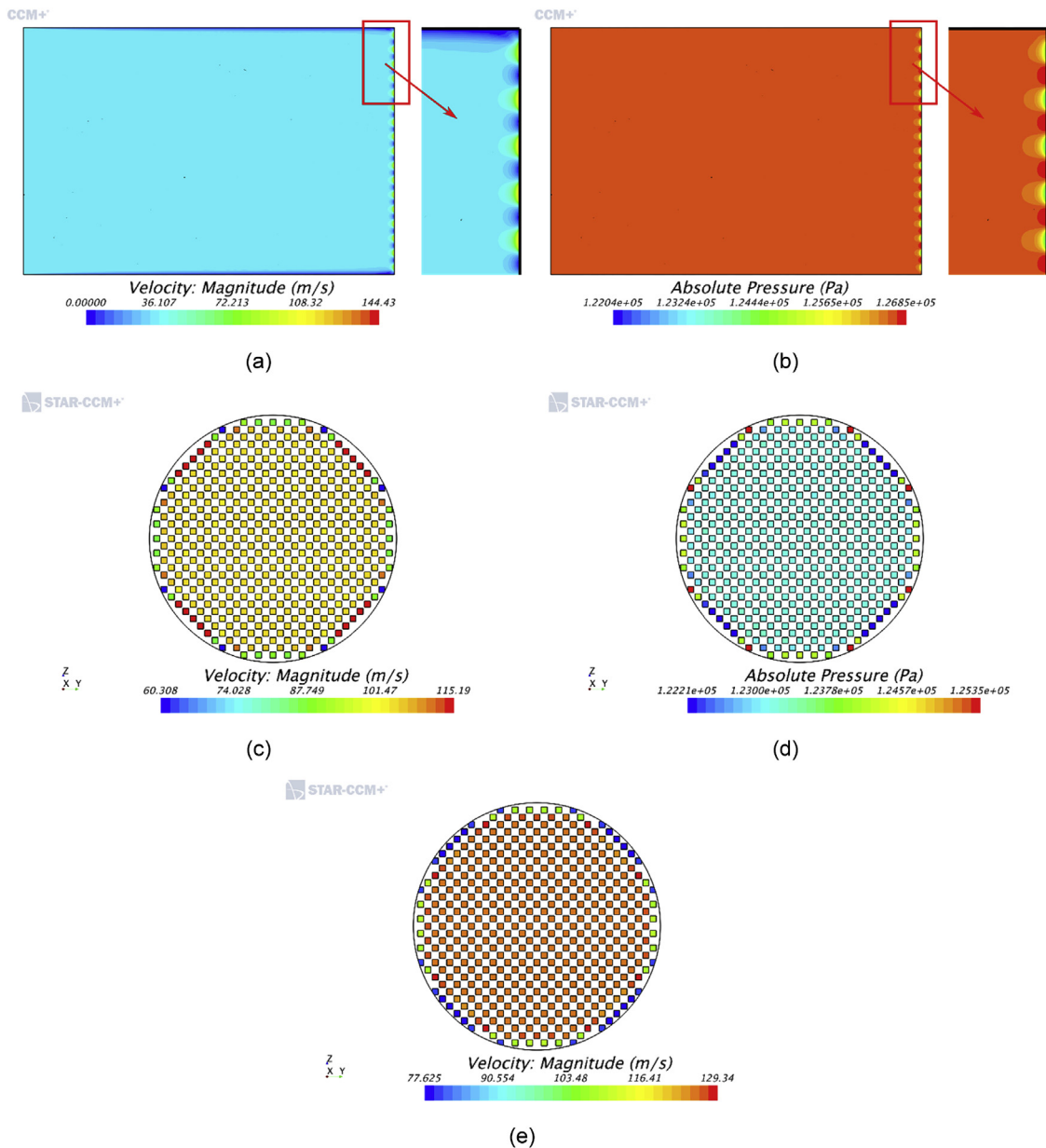
velocity and pressure distribution in the channels for different permeability values as shown in Ref. [5]. In a coated filter the velocity profile in the axial direction is almost linear, while in bare filters a sharp velocity gradient is present near the end of inlet channels and at the beginning of outlet channels, which requires a finer discretisation to be captured properly.

Figs. 6 and 7 show results for the bare and coated filter, respectively. In both cases, the velocity and pressure distribution upstream the filter (Figs. 6 and 7 (a) and (b)) are uniform up to a few millimetres away from the filter frontal face. Here, due to the change in section and smaller open frontal area the flow accelerates rapidly to enter the open channels while it forms small stagnation regions where the plugs are present. The pressure field reflects the velocity distribution, with a high stagnation pressure where the plugs are present and a lower pressure at the entrance of the open channels, where the flow is allowed to pass.

Figs. 6 and 7 (c) and (d) show the mean channel velocity and pressure at the entrance of each inlet channel. As expected, both velocity and pressure are mostly uniform at the entrance of the filter, except for a few cells located in the outer part of the filter. These cells may have either higher velocity and lower pressure or a lower velocity and higher pressure depending on their particular location, as this determines: 1) the number of cells with which one cell is connected and 2) how many impermeable walls each cell has. For example, looking at the 8 cells with the lowest velocity in Fig. 6 (c) it can be seen that they also have the highest backpressure from Fig. 6 (d). These cells have two porous walls and two impermeable walls and, hence, are only coupled with only two other cells each. Since all of the mass flow entering these cells is forced to pass through two porous walls only, instead of three or four as in other cells, the velocity through the porous wall will be higher and thus, in accordance with Darcy's law, the resulting pressure drop increases.

Comparing Figs. 6 and 7 (c), it is also interesting to notice that the flow distribution between the channels is more non-uniform in the bare filter. This could be attributed to the fact that in the bare filter the wall permeability is higher and thus the cross-flow between channels is more

(a)

(b)

(c)

(d)
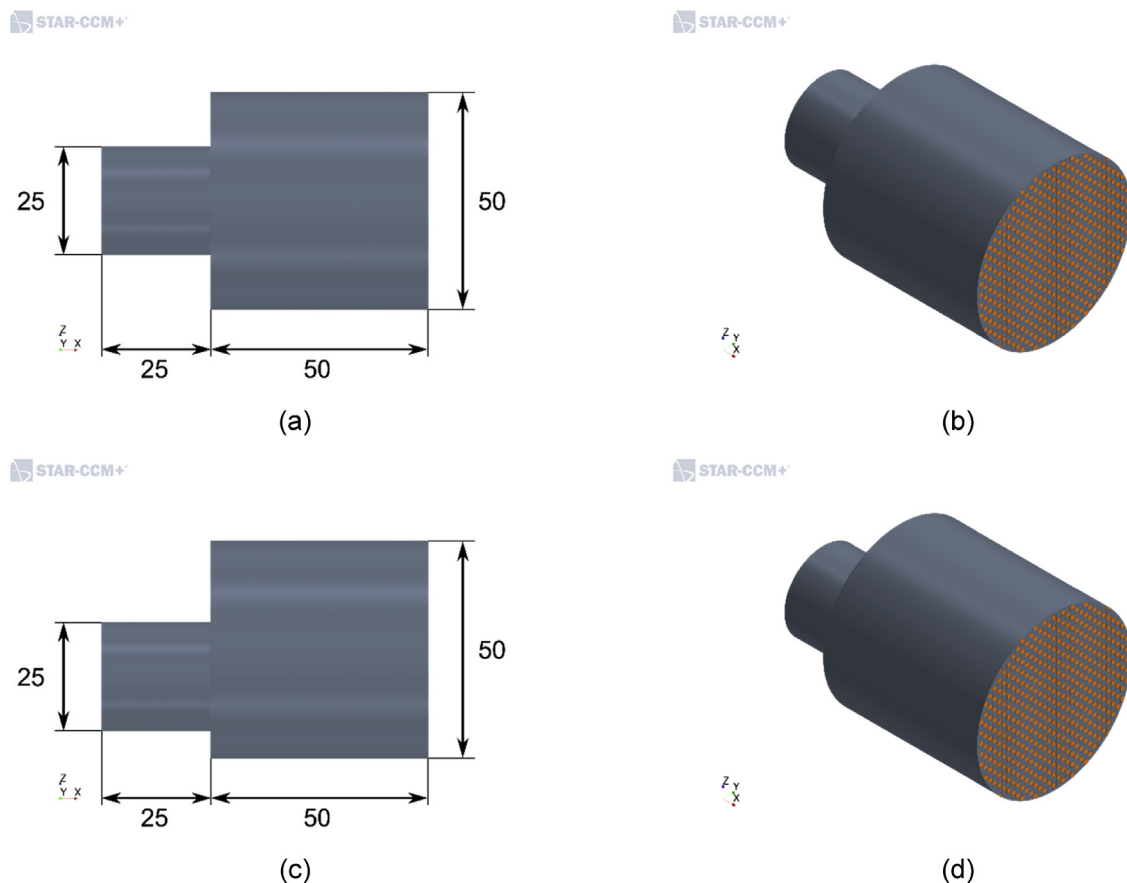
Fig. 8. Side and isometric views of the computational domains for concentric expansion case (a)–(b) and eccentric expansion case (c)–(d). Dimensions in [mm].

likely to be promoted.

Figs. 6 and 7 (e) show the mean channel velocity at the exit of each outlet channel. The outlet velocity shows the same qualitative trend of the inlet, but its magnitude is higher. This reflects the fact that as the flow advances through the channels its local pressure decreases and so does the density. Thus, in accordance with the conservation of mass, the magnitude of the velocity increases towards the end of the filter.

Finally, the total pressure drop of the two filters has been compared with the experimental data published in Ref. [5]. The total pressure drop of the bare filter is in good agreement with the experimental data, with a difference of about 7.5%, which is within the experimental uncertainty, while the total pressure drop of the coated filter is about 16% higher with respect the experimental data, which is slightly outside the experimental uncertainty. The fact that the coated filter shows a less accurate agreement with respect to the bare filter could be attributed to the non-uniform permeability in different filter channels in the experiments, caused by the non-uniform catalyst coating distribution.

Coated filter with upstream concentric and eccentric contraction

The flow upstream aftertreatment systems is very seldom uniform or even symmetrical. Apart from a sudden expansion, the inlet pipe is often not aligned with the monolith axis, and other factors (such as a 90-degree bend, for example) will affect upstream flow symmetry. In this section, the effect of a sudden expansion and asymmetry upstream of the filter is considered, using two catalyst coated filters with a concentric and an eccentric expansion upstream (Fig. 8). In the case with the eccentric expansion the inlet section axis is shifted 6.25 [mm] (half the inlet section radius) away from the expansion axis. Filter geometry and permeability are the same as those reported in Table 2 for the coated filter.

Figs. 9 and 10 show results of the concentric and eccentric expansion

cases, respectively.

In both cases, the velocity and pressure distribution upstream the filter (Figs. 9 and 10 (a) and (b)) are non-uniform. It is evident that the non-uniformity is caused by the "jet" that develops when the flow is discharged in the expansion section and impinges the filter frontal face.

In the concentric expansion case (Fig. 9 (a) and (b)) the flow distribution is similar to a sudden expansion with a catalytic converter, as discussed, for example, in Ref. [21]. As the flow approaches the filter, a region with adverse pressure gradient is generated, which forces the flow to deflect towards the outside. In the impingement region, the flow that is about to enter the filter channels is mainly axial. As expected, due to the sudden expansion, the flow separates from the expansion walls, forming a shear layer region between the jet and the recirculation region.

Fig. 9 (c) and (d) show the mean channel velocity and pressure at the entrance of each inlet channel. It can be seen that both velocity and pressure are again non-uniform at the entrance of the filter. Here the magnitude of the flow velocity is more than 10% higher in the central part, where the main flow impinges the filter, than in the outer region, and the same qualitative trend is visible for the pressure. The velocity non-uniformity is then preserved as the flow progresses through the channels towards the end of the filter, as shown by Fig. 9 (e). Due to the change in density along the filter, as discussed in the previous section, the velocity magnitude at the outlet is higher than that at the inlet.

The eccentric expansion case shows similar features to the concentric case, and thus only the differences between the two are highlighted here. The first visible difference is the shape of the separation zone at the expansion wall. It is considerably smaller at the wall nearest to the inlet pipe, as would be expected (Fig. 10 (a)). However, the "jet" behaviour is slightly more complex than just a shift caused by the shift of the inlet pipe. The jet is slightly diverted towards the nearest wall. As the main flow approaches the filter a high pressure area is present at the
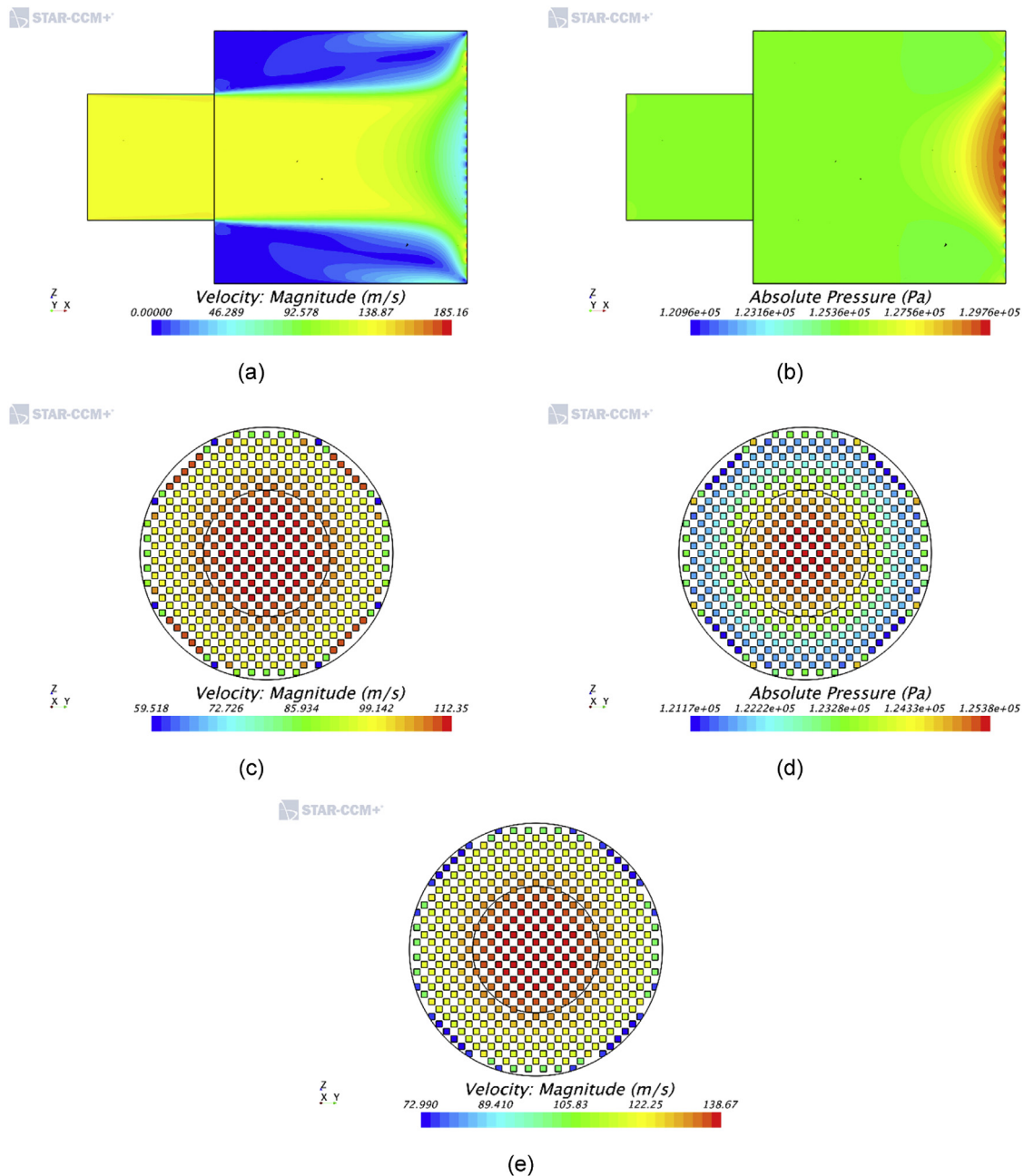
Fig. 9. Results for 300/8 coated filter with concentric expansion: (a) Velocity magnitude in the mid-section of the CFD domain (with the flow going from the left to the right), (b) Absolute pressure in the mid-section of the CFD domain, (c) Mean channel velocity at the entrance of each inlet channel (from the Matlab domain), (d) Mean channel pressure at the entrance of each inlet channel (from the Matlab domain), (e) Mean channel velocity at the exit of each outlet channel (from the Matlab domain).

impingement region aligned with the inlet pipe axis. A smaller pressure peak is present next to it at the wall nearest to the inlet pipe axis (Fig. 10 (b)). This is caused by the flow encountering the high resistance at the front face of the filter and thus directed towards the diffuser wall, where it impinges on the side wall of the diffuser causing another stagnation pressure peak.

Fig. 10 (c) and (d) show the non-uniform distribution of velocity and pressure at the entrance of the filter, while Fig. 10 (e) shows the non-uniform distribution of velocity at the exit of the filter. Here, similarly to the previous case, the velocity magnitude of the flow is more than 10% higher in the high pressure areas than in the region surrounding them.

The results of these two cases show that, although the high back-pressure from the filter tends to flatten the flow profile, a highly non-uniform flow profile upstream will result in non-uniform flow distribution between the filter channels. This means that a higher mass flow rate will be observed in some of the channels and thus will cause higher soot and ashes accumulation, changing the filter performance.

Coated filter with uneven permeability

As discussed before, non-uniformity in the flow distribution between filter channels can be also caused by non-uniform properties between channels, such as wall thickness (due to soot/ash accumulation), wall permeability (due to soot/ash accumulation and uneven catalyst coating) or other factors such as manufacturing defects. In this section, the focus is on the effect of non-uniform wall permeability between different channels. Two upstream flow configurations are considered, one without sudden expansion upstream (as in Fig. 5) and one with a concentric
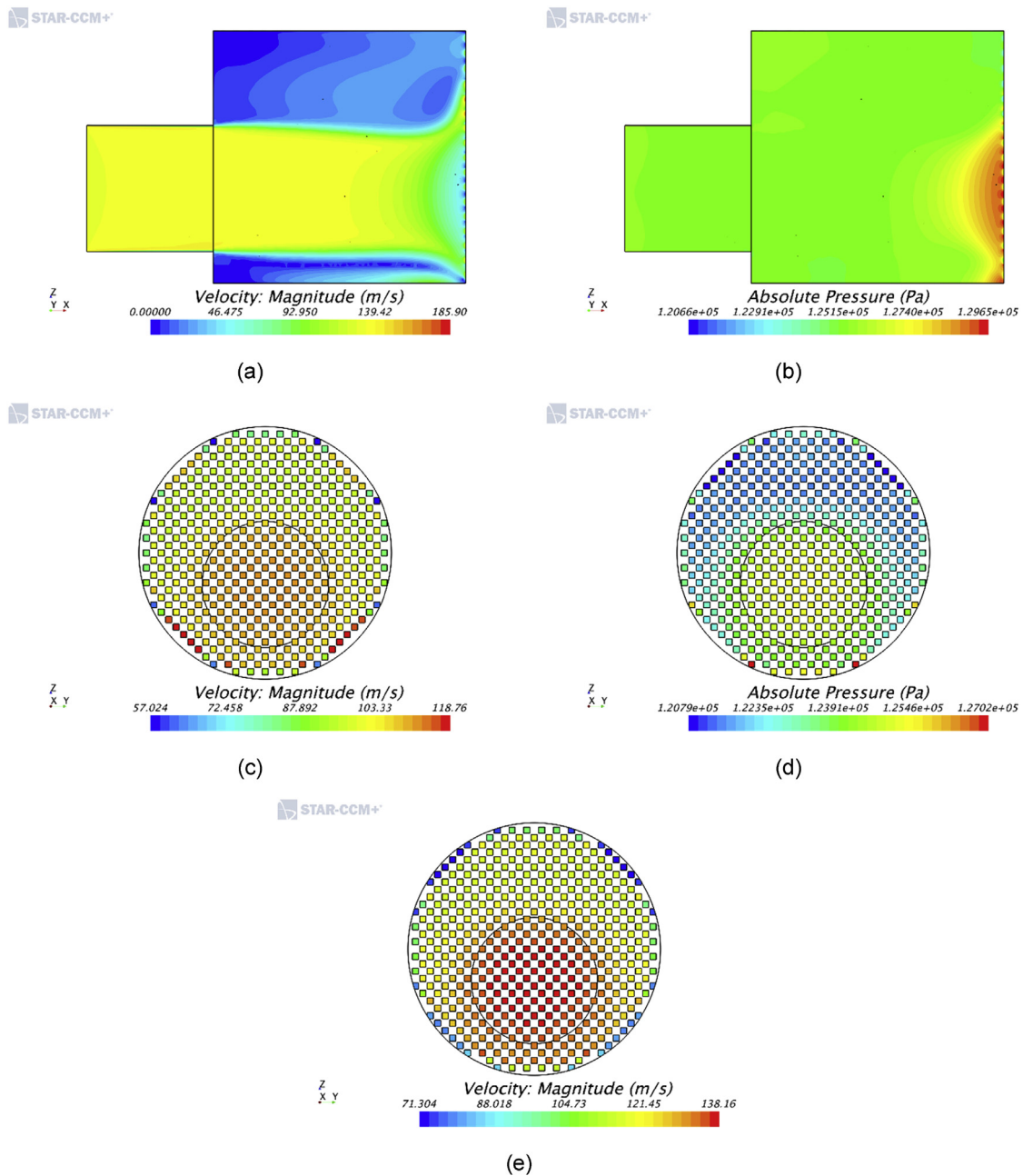
Fig. 10. Results for 300/8 coated filter with eccentric expansion: (a) Velocity magnitude in the mid-section of the CFD domain (with the flow going from the left to the right), (b) Absolute pressure in the mid-section of the CFD domain, (c) Mean channel velocity at the entrance of each inlet channel (from the Matlab domain), (d) Mean channel pressure at the entrance of each inlet channel (from the Matlab domain), (e) Mean channel velocity at the exit of each outlet channel (from the Matlab domain).

expansion (as in Fig. 8 (a) and (b)).

The filter geometry is the same as the one reported in Table 2 for the coated filter, while a permeability of $k_{out} = 2.09 \times 10^{-13}\ [m^2]$ (10% higher than the value reported in Table 2) has been assigned in the outer region of the filter and a permeability of $k_{in} = 1.71 \times 10^{-13}\ [m^2]$ (10% lower than the value reported in Table 2) has been assigned in the inner region, as shown in Fig. 11.

Figs. 12 and 13 show the results for the case without expansion upstream and the case with the concentric expansion, respectively. Velocity magnitude and absolute pressure at the mid-section of the CFD domain are not shown as they present similar features to the respective cases with homogeneous permeability, which have been already discussed.

It can be seen from Fig. 12 (a) and (b) that, in the case without expansion, the lower permeability in the central part causes a higher

resistance to the flow, which is diverted towards the outer region. Thus, the flow distribution becomes less uniform with respect to the case with homogeneous permeability. Moreover, Fig. 12 (c) shows that the non-uniformity of the flow is preserved at the filter exit.

Also in the case with the concentric expansion the lower permeability in the central part causes the flow to divert towards the outer region. However, since the lower permeability region coincides with the "jet" impingement region, the higher resistance in the central part results in flow deceleration and thus helps the flow to become more uniform, as evident from a comparison between Figs. 13 (b) and 9 (c).

It is interesting to notice that the overall filter pressure drop for both these cases is lower than the corresponding cases with homogeneous permeability. This can be explained by the fact that there is a higher mass flow entering the channels with higher permeability, which provide a
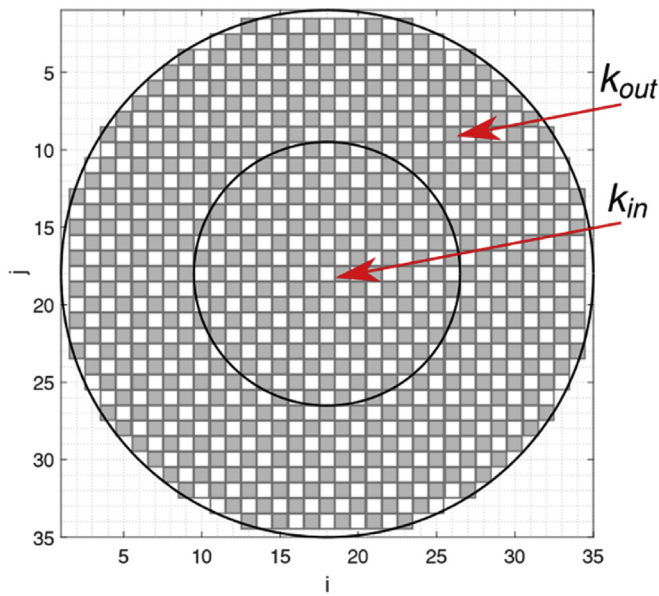
Fig. 11. A schematic of the non-uniform permeability distribution.

lower resistance.

This finding would explain why the pressure drop for the coated filter predicted with the multi-channel approach and uniform permeability shows a higher value than the experimental results published in Ref. [5].

The results for these two cases show that the non-homogeneous permeability affects the flow distribution in the filter, and

consequently soot and ashes accumulation, and that this might or might not be beneficial in terms of flattening the flow profile depending on the particular configuration upstream of the filter.

Total pressure drop

Total pressure drop across the filter has been calculated for all cases as discussed in the methodology section and is presented in Table 3. Although it has been shown that the non-uniform upstream flow is not flattened by the presence of the filter, the results for the coated filter with homogeneous permeability seem to show that this has little effect on the total pressure drop. The effect of non-uniform permeability seems to be, however, more pronounced with the resulting pressure drop which is about 2% lower than that with the uniform permeability. Nevertheless, a larger expansion ratio or a shorter expansion section might change these results and would require further investigation. Similarly, different permeability distribution between the channels may result in more pronounced pressure drop differences.

It is also reasonable to assume that as the three configurations investigated here provide three different flow distributions, their respective soot and ash accumulation patterns, and hence filter local permeability, will be different. Consequently, it is likely that after a short period of loading, filters with different upstream configurations will provide different total pressure drops.

Superficial velocity in the wall

One of the advantages of the proposed approach is detailed information about axial flow and pressure distribution in all channels. In particular, superficial velocity distribution analysis through the wall can
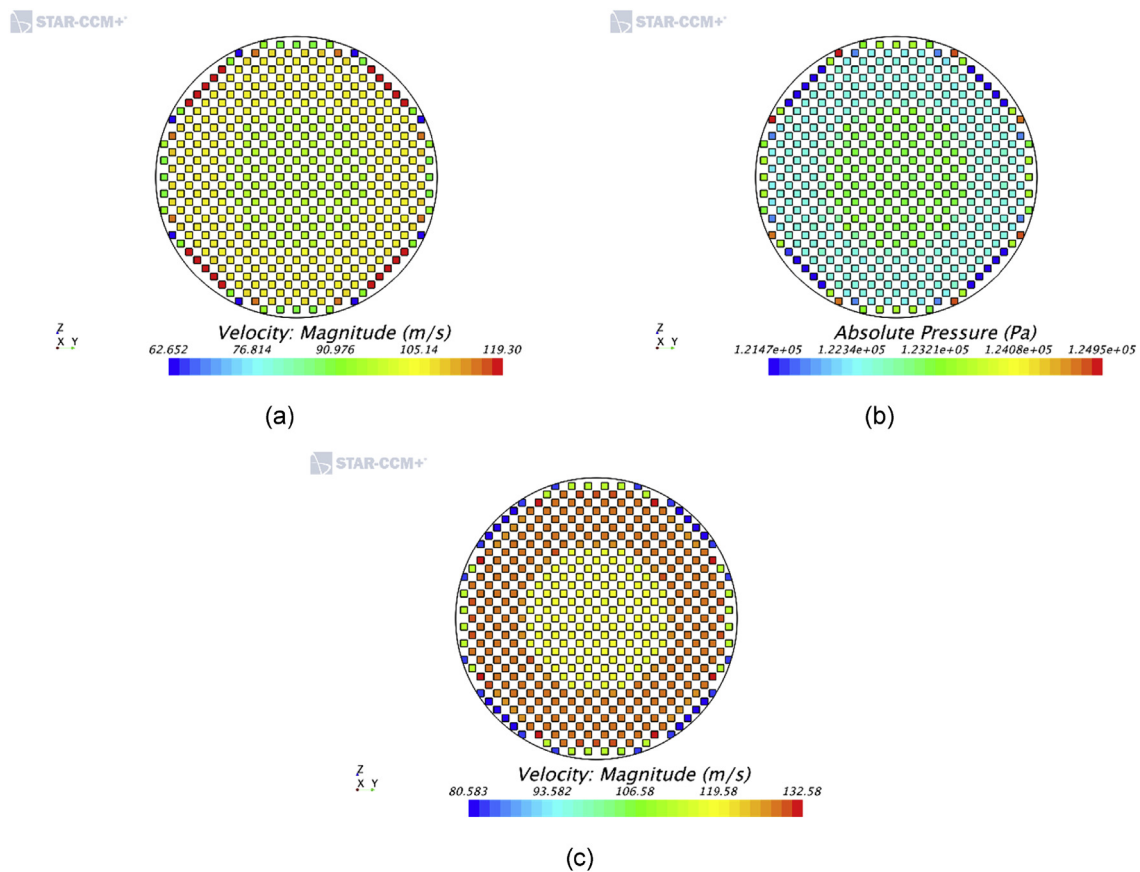

(a)

(b)

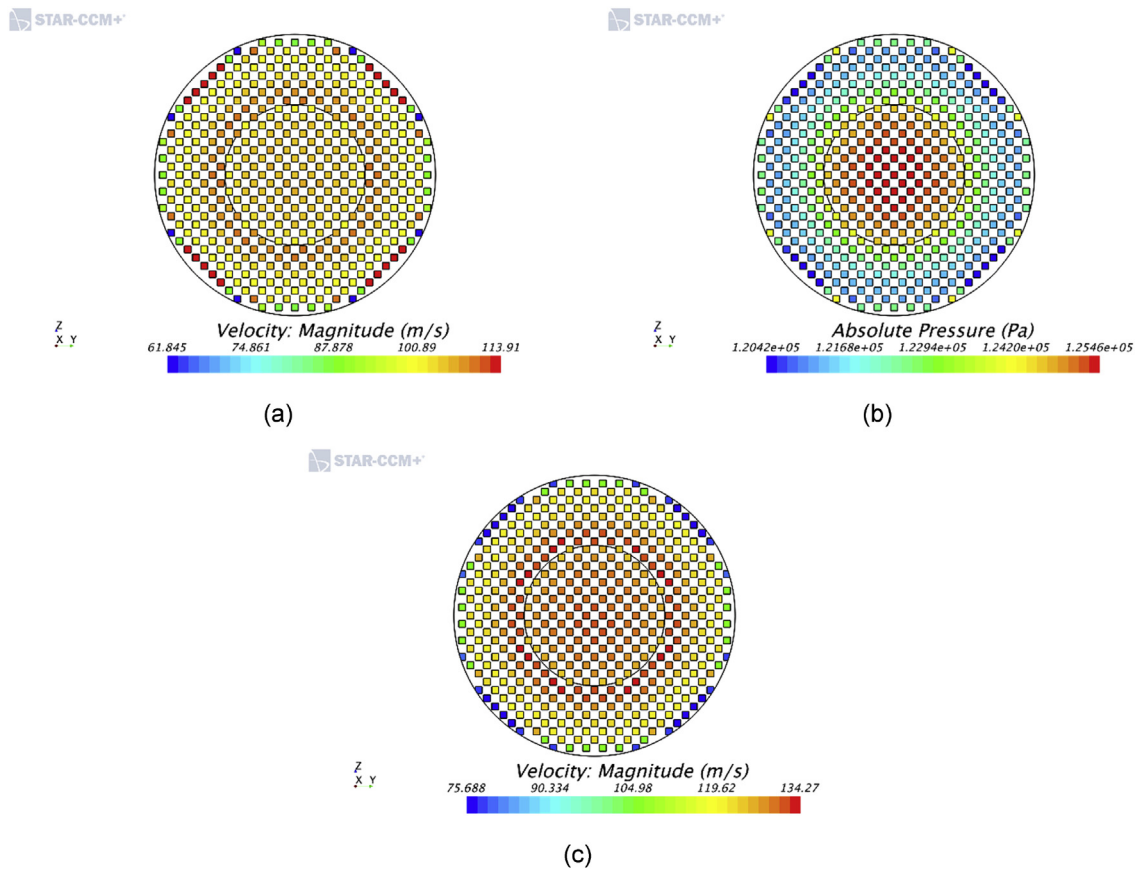
(c)

Fig. 12. Results for 300/8 coated filter without expansion in front of the filter and with non-homogeneous permeability: (a) Mean channel velocity at the entrance of each inlet channel (from the Matlab domain), (b) Mean channel pressure at the entrance of each inlet channel (from the Matlab domain), (c) Mean channel velocity at the exit of each outlet channel (from the Matlab domain).

(a)

(b)

(c)

Fig. 13. Results for 300/8 coated filter with concentric expansion in front of the filter and non-homogeneous permeability: (a) Mean channel velocity at the entrance of each inlet channel (from the Matlab domain), (b) Mean channel pressure at the entrance of each inlet channel (from the Matlab domain), (c) Mean channel velocity at the exit of each outlet channel (from the Matlab domain).

Table 3
Total pressure drop across the filter cores.

Filter	Upstream Configuration	Permeability	Total Pressure Drop
300/8 Bare	Without expansion	Homogeneous	9.9 [kPa]
300/8 Coated	Without expansion	Homogeneous	23.8 [kPa]
300/8 Coated	Concentric expansion	Homogeneous	23.8 [kPa]
300/8 Coated	Eccentric expansion	Homogeneous	23.8 [kPa]
300/8 Coated	Without expansion	Non-homogeneous	23.3 [kPa]
300/8 Coated	Concentric expansion	Non-homogeneous	23.4 [kPa]

help in predicting the location of the soot accumulation. This will be very beneficial when the model is extended to transient regime, which is the subject of future work.

To illustrate how the model can help in analysis of filter efficiency, two pairs of channels have been selected at the centre of the filter (Ch2) and next to the outer wall (Ch1). Fig. 14 shows superficial velocities for the case without expansion upstream of the filter and non-homogeneous permeability, while Fig. 15 refers to the case with the concentric expansion upstream the filter and homogeneous permeability. Here left, right, top and bottom superficial velocities refer to the velocity magnitude between the central cell and neighbouring cells as shown in Fig. 2.

Fig. 14 (a) compares the superficial velocities in the outer inlet channel (Ch 1) with the central one (Ch 2). While in the centre of the filter (Ch2) all four superficial velocities are the same, near the wall there is a noticeable difference between the flow through different walls (note that the top velocity in Ch1 is zero as there is no neighbouring cell there). In both channels the superficial velocities are increasing from the beginning of the filter towards the end, showing that a higher percentage

of the flow passes from the inlet to the outlet channel in the second half of the filter. This effect is more pronounced in the central channel.

Fig. 14 (b) compares the superficial velocities in the outlet channels near the wall (Ch 1) and near the centre of the filter (Ch 2). Here the velocity trends are similar to the inlet channels, however the magnitudes are higher. This is caused by the density difference between the inlet and outlet channels, as discussed before.

In case with homogeneous permeability and a sudden expansion (Fig. 15 (a) and (b)) the superficial velocity trends are the same. Here the difference in superficial velocities between the central and peripheral channel is bigger, which reflects the fact that the flow is much more non-uniform.

Conclusion

This paper presents a method for multi-channel simulations of flow in particulate filters based on the 1-dimensional formulation from Konstandopoulos [19]. Full flow coupling between the channels has been
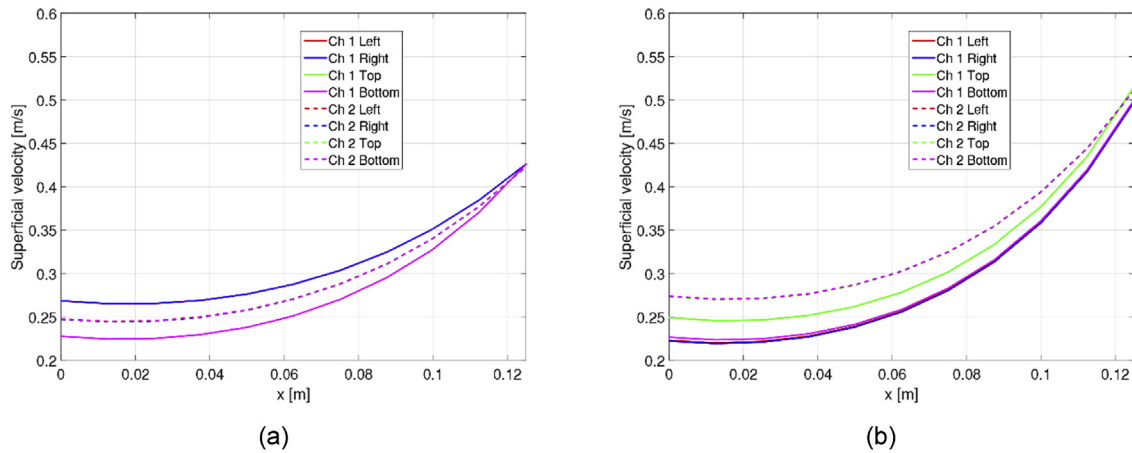
Fig. 14. Superficial velocity magnitude along the filter axial direction for the 300/8 coated filter without expansion and with non-homogeneous permeability: (a) Inlet channel and (b) outlet channel. (Superficial velocities in Ch 2 are overlapping).
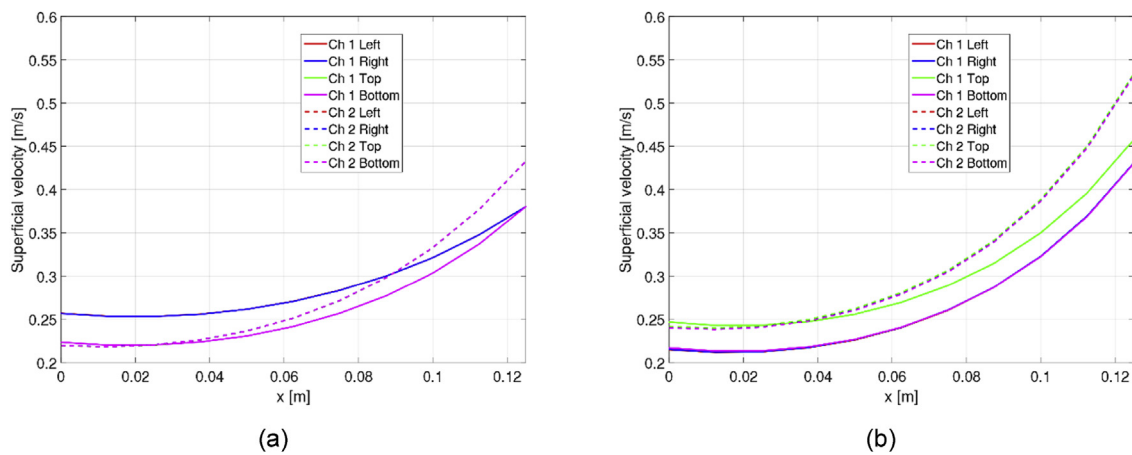

Fig. 15. Superficial velocity magnitude along the filter axial direction for the 300/8 coated filter with concentric expansion and homogeneous permeability: (a) Inlet channel and (b) outlet channel. (Superficial velocities in Ch 2 are overlapping).

implemented and coupling between fully 3-dimensional upstream flow and multi-channel filter flow model has been demonstrated by using Matlab and StarCCM+. The model accounts for local density changes in the channels and inside the porous walls, and provides full flexibility in prescription of individual channel properties (wall thickness, hydraulic diameter and wall permeability).

Several representative geometries were considered, featuring non-uniform flow caused by the upstream geometry (such as a symmetric or asymmetric sudden expansion) and channel properties (different permeability in different areas of the filter). It has been shown that upstream flow non-uniformity may persist through the filter, which needs to be taken into account in filter design. The effect of different wall permeability between different channels has also been demonstrated.

The model provides not only global flow parameters such as the total pressure drop across the filter, but also offers insight into flow and pressure distribution along the channel axis, which is important for heat transfer, soot and ash accumulation studies. By varying wall thickness and/or permeability in the axial direction, the effect of the soot accumulation and uneven catalyst coating distribution can also be considered.

While the model presented here is based on the laminar flow formulation, which is adequate for a wide range of filter operation parameters, it can also be extended to the turbulent regime by including turbulent friction factor as described in Ref. [5]. Heat transfer can be included by using local temperature for density calculations and adding energy conservation equation. In the current formulation of the model, different wall thickness and channel hydraulic diameter can be provided for different channels, however this would require modification of the Darcy losses because of the cross-sectional area changes in the walls between channels of different hydraulic diameters. This will be incorporated in the future. Together with modifications for transient flows, this would allow studies of soot and ash accumulation on the filter walls to be performed. Finally, coupling with a downstream CFD solution would be reasonably straightforward and can be performed following an approach similar to that presented here.

Author contribution

Appendix

Derivation of Eq. (3) – (6)

In order to account for the pressure variation across the porous wall, the differential form of the Darcy's law can be used:

$$dP = \frac{\mu}{k} u_w \, dw \tag{A.1}$$

Here dP is the pressure difference between two points inside the wall, dw is the distance between these two points, and u_w is the average superficial wall velocity in the considered interval, as shown in Fig. 16

Eq. (A.1) is multiplied by $P(x)$:

$$PdP = \frac{\mu}{k} (u_w P) \, dw \tag{A.2}$$

and integrated with respect to w:

$$\int_{P_1}^{P_2} PdP = \int_{0}^{w_s} \frac{\mu}{k} (u_w P) \, dw \tag{A.3}$$

Viscosity can be considered constant, and the product $u_w P = u_w \rho R_{Gas} T = \dot{m} \frac{R_{Gas} T}{A}$ is proportional to the mass flow through the wall (here A is a cross-section of the wall), therefore is also constant for constant temperature across the wall, therefore we can integrate (A.3) to get:

$$\frac{P_2^2 - P_1^2}{2} = \frac{\mu}{k} (u_w P) \, w_s \tag{A.4}$$

Rearranging this expression gives:

$$(P_2 - P_1) = P \left(\frac{2}{P_2 + P_1} \right) \frac{\mu}{k} w_s u_w \tag{A.5}$$

Here product $Pu_w = P_1 u_{w1} = P_2 u_{w2}$ can be evaluated at any wall cross-section as it is assumed to be constant for a constant wall temperature.
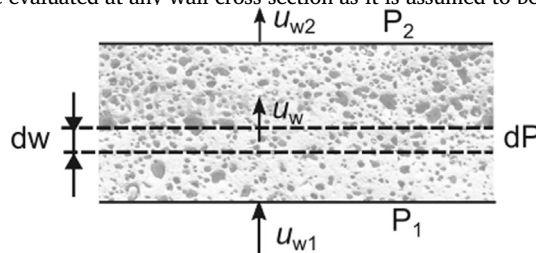

Fig. 16. Notation used in derivation of the Darcy law.

Derivation of Eqs. (8) and (9)

Expressing wall velocities v and w from Eq. (3) – (6) and substituting them into Eq. (1) yields:

$$\frac{d}{dx}\left(\rho_{i,j} u_{i,j}\right) = -\xi \frac{1}{d_h} \rho_{i,j} \frac{1}{\xi P_{i,j}} \left(\frac{\left(P_{i,j}^2 - P_{i-1,j}^2\right)}{2} \frac{\tau_{i,j}}{\mu \, t_{i,j}} + \frac{\left(P_{i,j}^2 - P_{i,j-1}^2\right)}{2} \frac{\sigma_{i,j}}{\mu \, s_{i,j}} + \frac{\left(P_{i,j}^2 - P_{i+1,j}^2\right)}{2} \frac{\tau_{i+1,j}}{\mu \, t_{i+1,j}} + \frac{\left(P_{i,j}^2 - P_{i,j+1}^2\right)}{2} \frac{\sigma_{i,j+1}}{\mu \, s_{i,j+1}} \right) \tag{A.6}$$

Using Eq. (7) for the density and rearranging gives

$$\frac{d}{dx}\left(\frac{P_{i,j}}{R_{Gas} T} u_{i,j}\right) = -\frac{1}{d_h} \frac{1}{R_{Gas} T} \frac{1}{2\mu} \left(\left(P_{i,j}^2 - P_{i-1,j}^2\right) \frac{\tau_{i,j}}{t_{i,j}} + \left(P_{i,j}^2 - P_{i,j-1}^2\right) \frac{\sigma_{i,j}}{s_{i,j}} + \left(P_{i,j}^2 - P_{i+1,j}^2\right) \frac{\tau_{i+1,j}}{t_{i+1,j}} + \left(P_{i,j}^2 - P_{i,j+1}^2\right) \frac{\sigma_{i,j+1}}{s_{i,j+1}} \right) \tag{A.7}$$

Assuming that the temperature is uniform in the channel, the left hand side can be differentiated:

$$P_{i,j} \frac{d}{dx}\left(u_{i,j}\right) + u_{i,j} \frac{d}{dx}\left(P_{i,j}\right) = -\frac{1}{d_h} \frac{1}{2\mu} \left(\left(P_{i,j}^2 - P_{i-1,j}^2\right) \frac{\tau_{i,j}}{t_{i,j}} + \left(P_{i,j}^2 - P_{i,j-1}^2\right) \frac{\sigma_{i,j}}{s_{i,j}} + \left(P_{i,j}^2 - P_{i+1,j}^2\right) \frac{\tau_{i+1,j}}{t_{i+1,j}} + \left(P_{i,j}^2 - P_{i,j+1}^2\right) \frac{\sigma_{i,j+1}}{s_{i,j+1}} \right) \tag{A.8}$$

Thus, the first derivative of $u_{i,j}$ can be expressed as

$$\frac{d}{dx}\left(u_{i,j}\right) = -\frac{1}{P_{i,j}} u_{i,j} \frac{d}{dx}\left(P_{i,j}\right) - \frac{1}{P_{i,j}} \frac{1}{d_h} \frac{1}{2\mu} \left(\left(P_{i,j}^2 - P_{i-1,j}^2\right) \frac{\tau_{i,j}}{t_{i,j}} + \left(P_{i,j}^2 - P_{i,j-1}^2\right) \frac{\sigma_{i,j}}{s_{i,j}} + \left(P_{i,j}^2 - P_{i+1,j}^2\right) \frac{\tau_{i+1,j}}{t_{i+1,j}} + \left(P_{i,j}^2 - P_{i,j+1}^2\right) \frac{\sigma_{i,j+1}}{s_{i,j+1}} \right), \tag{A.9}$$

Similarly, the expression for density (Eq. (7)) can be used in the momentum balance Eq. (2):

$$\frac{d}{dx}\left(\frac{P_{i,j}}{R_{Gas} T} u_{i,j}^2\right) = -\frac{d}{dx}\left(P_{i,j}\right) - 2fRe \frac{\mu}{d_h^2} u_{i,j} \tag{A.10}$$

For isothermal channel flow, the left hand side can be differentiated to get

$$\frac{1}{R_{Gas}T}u_{i,j}^2\frac{d}{dx}\left(P_{i,j}\right) + \frac{2}{R_{Gas}T}P_{i,j}u_{i,j}\frac{d}{dx}\left(u_{i,j}\right) = -\frac{d}{dx}\left(P_{i,j}\right) - 2fRe\frac{\mu}{d_h^2}u_{i,j} \tag{A.11}$$

Therefore the first derivative of the pressure $P_{i,j}$ can be expressed as:

$$\frac{d}{dx}\left(P_{i,j}\right) = \frac{1}{\left(1 + \frac{1}{R_{Gas}T}\,u_{i,j}^2\right)}\left(-\frac{2}{R_{Gas}T}P_{i,j}u_{i,j}\frac{d}{dx}\left(u_{i,j}\right) - 2fRe\frac{\mu}{d_h^2}u_{i,j}\right) \tag{A.12}$$

Finally, substituting Eq. (A.12) into Eq. (A.9) and rearranging gives Eq. (8):

$$\frac{d}{dx}\left(u_{i,j}\right) = \frac{1}{\left(1 - \frac{1}{1+\frac{1}{R_{Gas}T}u_{i,j}^2}\frac{2}{R_{Gas}T}\,u_{i,j}^2\right)}\left[\frac{1}{P_{i,j}}\left(\frac{1}{1+\frac{1}{R_{Gas}T}u_{i,j}^2}\right)2fRe\frac{\mu}{d_h^2}u_{i,j}^2 - \frac{1}{P_{i,j}}\frac{1}{d_h}\frac{1}{2\mu}\left(\frac{\tau_{i,j}}{t_{i,j}}\left(P_{i,j}^2 - P_{i-1,j}^2\right) + \frac{\sigma_{i,j}}{s_{i,j}}\left(P_{i,j}^2 - P_{i,j-1}^2\right) + \frac{\tau_{i+1,j}}{t_{i+1,j}}\left(P_{i,j}^2 - P_{i+1,j}^2\right) + \frac{\sigma_{i,j+1}}{s_{i,j+1}}\left(P_{i,j}^2 - P_{i,j+1}^2\right)\right)\right] \tag{A.13}$$

and substituting Eq. (A.13) into Eq. (A.12) and rearranging gives Eq. (9):

$$\frac{d}{dx}\left(P_{i,j}\right) = \frac{1}{1+\frac{1}{R_{Gas}T}u_{i,j}^2}\left\{-\frac{2}{R_{Gas}T}P_{i,j}u_{i,j}\left\{\frac{1}{\left(1-\frac{1}{1+\frac{1}{R_{Gas}T}u_{i,j}^2}\frac{2}{R_{Gas}T}\,u_{i,j}^2\right)}\left[\frac{1}{P_{i,j}}\left(\frac{1}{1+\frac{1}{R_{Gas}T}u_{i,j}^2}\right)2fRe\frac{\mu}{d_h^2}u_{i,j}^2\right.\right.\right.$$

$$\left.\left.\left. - \frac{1}{P_{i,j}}\frac{1}{d_h}\frac{1}{2\mu}\left(\frac{\tau_{i,j}}{t_{i,j}}\left(P_{i,j}^2 - P_{i-1,j}^2\right) + \frac{\sigma_{i,j}}{s_{i,j}}\left(P_{i,j}^2 - P_{i,j-1}^2\right) + \frac{\tau_{i+1,j}}{t_{i+1,j}}\left(P_{i,j}^2 - P_{i+1,j}^2\right) + \frac{\sigma_{i,j+1}}{s_{i,j+1}}\left(P_{i,j}^2 - P_{i,j+1}^2\right)\right)\right]\right\} - 2fRe\frac{\mu}{d_h^2}u_{i,j}\right\} \tag{A.14}$$

References

[1] R. Niessner, The many faces of soot: characterization of soot nanoparticles produced by engines, Angew. Chem. Int. Ed. 53 (46) (2014) 12366–12379, https://doi.org/10.1002/anie.201402812.

[2] İ.A. Reşitoğlu, K. Altinişik, Ali Keskin, "The pollutant emissions from diesel-engine vehicles and exhaust aftertreatment systems," Clean Techn, Environ. Policy 17 (2015) 15–27, https://doi.org/10.1007/s10098-014-0793-9.

[3] J. Tollefson, Soot a major contributor to climate change, Nature News (2013), https://doi.org/10.1038/nature.2013.12225, 15th Jan.

[4] A.J. Torregrosa, J.R. Serrano, F.J. Arnau, P. Piqueras, A fluid dynamic model for unsteady compressible flow in wall-flow diesel particulate filters, Enegry 36 (2011) 671–684, https://doi.org/10.1016/j.energy.2010.09.047.

[5] M. Prantoni, S. Aleksandrova, H. Medina, J. Saul, F. Benjamin, O. Garcia Afonso, Modelling pressure losses in gasoline particulate filters in high flow regimes and temperatures, JSAE 20199166 (2019) (in-press).

[6] E.J. Bissett, Mathematical Model of the Thermal Regeneration of a wall-flow monolith diesel particulate filter, Chem. Eng. Sci. 39 (1984) 1233–1244, https://doi.org/10.1016/0009-2509(84)85084-8.

[7] G. Koltsakis, O. Haralampous, C. Depcik, J.C. Ragone, Catalyzed diesel particulate filter modeling, Rev. Chem. Eng. 29 (1) (2013) 1–61, https://doi.org/10.1515/revce-2012-0008.

[8] S. Yang, C. Deng, Y. Gao, Y. He, Diesel particulate filter design simulation: a review, Adv. Mech. Eng. 8 (3) (2016) 1–14, https://doi.org/10.1177/1687814016637328.

[9] C. Depcik, B. Spickler, A. Gaire, Revisiting the single equation pressure drop model for particulate filters, SAE Int. J. Engines (2018), https://doi.org/10.4271/2018-01-0952, 2018-01-0952.

[10] G. Gong, M.L. Stewart, A. Zelenyuk, A. Strzelec, S. Viswanathan, D.A. Rothamer, D.E. Foster, C.J. Rutland, "Importance of filter's microstructure in dynamic filtration modelling of gasoline particulate filters (GPFs): inhomogeneous porosity and pore size distribution, Chem. Eng. J. 338 (2018) 15–26, https://doi.org/10.1016/j.cej.2018.01.006.

[11] S. Korneev, S. Onori, Modeling the transport dynamics in gasoline particulate filters, ASME Proc. (2018), https://doi.org/10.1115/DSCC2018-9160. V002T26A002.

[12] S. Aleksandrova, J. Saul, M. Prantoni, H. Medina, O. Garcia Afonso, M. Bevan, S. Benjamin, Turbulent flow pressure losses in gasoline particulate filters, SAE Int. J. Engines 12 (4) (2019) 455–470, https://doi.org/10.4271/03-12-04-0030.

[13] Koltsakis, G.C., Haralampous, O.A., Margaritis, N.K., Samaras, Z.C., Vogt, C.D., Ohara, E., Watanbe, Y. and Mizutani, T., "3-Dimensional modeling of the regeneration in SiC particulate filters," SAE Technical Paper, 2005-01-0953, doi: 10.4271/2005-01-0953

[14] G. Pozzato, M.A. Hoffman, S. Onori, Multi-channel physics-based modeling and experimental validation of an uncoated gasoline particulate filter in clean operating conditions, Am. Control Conf. (2017), https://doi.org/10.23919/ACC.2017.7963793.

[15] C. Depick, C. Langness, J. Mattson, Development of a Simplified Diesel Particulate Filter Model Intended for an Engine Control Unit, 2014, https://doi.org/10.4271/2014-01-1559. SAE Technical Paper, 2014-01-1559.

[16] A.G. Konstandopoulos, M. Kostoglou, P. Housiada, Spatial Non-uniformities in Diesel Particulate Trap Regeneration, 2001. SAE Technical Paper, 2001-01-0908.

[17] M. Kostoglou, P. Housiada, A.G. Konstandopoulos, Multi-channel simulation of regeneration in honeycomb monolithic diesel particulate filters, Chem. Eng. Sci. 58 (2003), https://doi.org/10.1016/S0009-2509(03)00178-7.

[18] C. Zhao, Y. Zhu, Y. Wang, S. Huang, Pressure Drop and Soot Regeneration Characteristics through Hexagonal and Square Cell Diesel Particulate Filters, 2017, https://doi.org/10.4271/2017-01-0979. SAE Technical Paper, 2017-01-0979.

[19] A.G. Konstandopoulos, H. Johnson, Wall-flow Diesel Particulate Filters – Their Pressure Drop and Collection Efficiency, 1989. SAE Technical Paper, 890405.

[20] G. Padula, J. Saul, S. Aleksandrova, H. Medina, S. Benjamin, A New Take on the Porous Medium Approach for Modelling Monoliths and Other Multiple Channel Devices, 2019. SAE Technical Paper 2019-24-0049.

[21] I.H. Bin Rusli, S. Aleksandrova, H. Medina, S. Benjamin, The Effect of Swirl on the Flow Uniformity in Automotive Exhaust Catalysts, 2017. SAE Technical Paper, 2017-01-2384.

[22] F. Piscaglia, G. Ferrari, A novel 1D approach for the simulation of unsteady reacting flows in diesel exhaust after-treatment systems, Energy 34 (12) (2009) 2051–2062, https://doi.org/10.1016/j.energy.2008.08.022.

[23] A.G. Konstandopoulos, Flow Resistance Descriptors for Diesel Particulate Filters: Definitions, Measurements and Testing, 2003. SAE Technical Paper, 2003-01-0846.

[24] L.F. Shampine, J. Kierzenka, A BVP solver that controls residual and error, J. Numer. Anal. Ind. Appl. Math. 3 (1–2) (2008), 27-14.
[25] J.A. Sullivan, Fluid Power: Theory and Applications, third ed., vol. 82, Prentice-Hall, 1989, ISBN 0-13-323080-5.
[26] B.R. Munson, D.F. Young, T.H. Okiishi, W.W. Huebsch, Fundamentals of Fluid Mechanics, sixth ed., Wiley, 2009, ISBN 978-0470-26284-9, pp. 415–425.

Nomenclature

A_1 : $[m^2]$, Filter open frontal area
A_2 : $[m^2]$, Filter total frontal area
D_{Filter}: $[m]$, Filter diameter
d_h: $[m]$, Cell hydraulic diameter
f: $[-]$, Fanning friction factor
k: $[m^2]$, Filter permeability
L: $[m]$, Filter length
$\dot{m}$: $[kg/s]$, Channel mean cross-sectional mass flow rate
$P_{Atm.}$: $[Pa]$, Atmospheric pressure
P: $[Pa]$, Local mean pressure in the channel
R_{Gas} : $\left[\frac{m^2}{K\,s^2}\right]$, Specific gas constant
$Re = \frac{\rho U d_h}{\mu}$: $[-]$, Reynolds number at the entrance of the inlet channel

s: $[m]$, Horizontal wall thickness
S: $[K]$, Constant in Sutherland's law
t: $[m]$, Vertical wall thickness
T: $[°C]$, Temperature
T_{ref}: $[K]$, Reference temperature in Sutherland' law
u: $[m/s]$, Mean cross-sectional axial velocity
v: $[m/s]$, Mean cross-sectional superficial velocity through the vertical porous wall
w: $[m/s]$, Mean cross-sectional superficial velocity through the horizontal porous wall
x: $[m]$, Axial coordinateGreek letters
$\zeta_{Contr.}$: $[-]$, Contraction loss coefficient
$\zeta_{Exp.}$: $[-]$, Expansion loss coefficient
μ: $[kg/(m\,s)]$, Dynamic viscosity
μ_{ref}: $[kg/(m\,s)]$, Reference dynamic viscosity in Sutherland's law
ξ: $[-]$, Coefficient equal to 1 for the inlet channels and -1 for the outlet channels
ρ: $[kg/m^3]$, Density
σ: $[m^2]$, Horizontal wall permeability
τ: $[m^2]$, Vertical wall permeabilitySubscript
i: Subscript for cell indexing
j: Subscript for cell indexingDefinitions, acronyms, abbreviations
CFD: Computational Fluid Dynamics
DPF: Diesel Particulate Filter
GPF: Gasoline Particulate Filter
PM: Particulate Matter